A Novel Coordinated Detection Method for Transmissive/Reflective Sensors against Strong In-band Interference

Jie Teng[a], Shaorong Wang[a,*] and Lin Jiang[b]

[a]*School of Electrical and Electronic Engineering, Huazhong University of Science and Technology, Wuhan, 430074, China*
[b]*Department of Electrical Engineering and Electronics, University of Liverpool, Liverpool, L69 3GJ, UK*

ARTICLE INFO

Keywords:
transmissive/reflective sensor
detection method against in-band interference
coordinated modulation
digital filtering algorithm
odd/even function properties
electromagnetic mold level detection

ABSTRACT

Accuracy of transmissive/reflective sensors is usually degraded by strong in-band interference, especially those with frequencies very close or even equal to that of the measured signal. To tackle this challenge, this paper proposes a novel detection method including three units: a coordinated modulator (CM), a high-performance analog narrow-band filter (ANBF), and a smart digital filtering algorithm (SDFA). The CM performs a mixed function of amplitude modulation and phase modulation, and is used to control the sensor's transmitter to circularly transmit the signal modulated according to the coordinated time-sequence requirement from the SDFA. The ANBF has a very narrow passband to make the analog signal sampled by the SDFA only include the measured signal and an in-band interfering component. The SDFA utilizes the properties of odd/even functions and the definitions of power in A.C. circuit to filter out the in-band interfering component, with the coordination of the CM and ANBF. Effectiveness of the proposed method is validated via simulations and laboratory tests setting up based on a real application case of electromagnetic mold level detection under mold-electromagnetic stirring operating condition. Test results show that the proposed method can effectively deal with strong in-band interfering signal with the frequency very close or even equal to that of the measured signal. In the total of 20000 simulation cases, attenuations of in-band interference can exceed -76 dB. Moreover, in the experimental tests under a condition of -40 dB signal-to-noise ratio, measurement errors of the amplitude of the measured signal can be achieved less than 1.88%.

1. Introduction

Transmissive/reflective sensors are widely used in various industrial fields, such as displacement sensing [1], surface topography measurement [2] and liquid level detection [3]. Generally, this type of sensor comprises of a transmitter and a receiver. In operation, the transmitter transmits a signal to the measurand. Then the receiver senses the measurand's physical variables as the measured signal, which is only the part of the transmitted signal transmitting through or being reflected from the measurand. And according to the characteristics of the measured signal, the transmitted signals with different properties like optical [4], electromagnetic [5] are commonly used.

In practice, transmissive/reflective sensor usually equips a band-pass filter to reject the frequency components out of the passband. Even so, the in-band interference contained in the passband cannot be removed and then results in inaccurate sensing values. To address this issue, a few time-domain and frequency-domain interference cancellation methods have been developed. To subtract the interference, the time-domain methods estimate amplitude, frequency and phase of the interfering signal and then generate a canceling signal with the same amplitude, the same frequency and the opposite phase of the interference. Different parameter estimation techniques have been used, such as FFT [6] [7] and the single-channel independent component analysis [8]. However, effectiveness of those methods heavily depends upon the estimation accuracy of the interference frequency. For example, in [9], it is pointed out that the method will fail when the estimation error of the frequency exceeds 0.04 Hz out of 50 Hz (0.08%).

The frequency-domain cancellation method uses spectral subtraction for application fields where the phase of the measured signal is not needed, such as vibration detection [10] and speech signal processing [11]. Effectiveness of the spectral subtraction method also relies on the accuracy of FFT. Alternative solutions are adaptive noise cancellation methods (ANC) based on the self-optimization of filter without requiring explicit parameter estimation, such as [12] [13]. And different self-optimization methods like LMS algorithm [14] [15] and stochastic gradient algorithm [16] are applied on the weight calculations of the ANC. [17] has demonstrated the ANC's cancellation over -60 dB on the interferences with a frequency far from that of the measured signal. However, when the frequency of the interference is very close or even equal to that of the measured signal, both spectral subtraction and the ANC will significantly attenuate the measured signal and cannot extract the accurate sensing value. Moreover, the results of the above methods are ineffective for cases with low SNR.

This paper proposes a novel detection method including three units in coordination: 1) a coordinated modulator used to control the transmitter to circularly transmit a signal modulated in the time sequence; 2) an analog narrow-band filter rejecting the contents except for the measured signal and an in-band interfering component; and 3) a smart digital filtering algorithm canceling the in-band interference based on the odd/even function properties. The design scheme, theo-

retical analysis and implementation of the whole proposed method are presented in details. The effectiveness of the proposed method is verified by simulation and experimental tests based on a real application case.

Main contributions of this paper are summarized as: 1) the proposed method provides a unique coordinated solution at the measurement system design level. It involves modulation techniques, analog filter, and digital signal processing; 2) the proposed method utilizes the odd/even functions to cancel the in-band interference. This novel cancellation solves the failure due to estimation error of the interference frequency; 3) the proposed method extracts the measured signal based on power definitions in A.C. circuit, which makes it possible to obtain the phase delay of the measured signal; 4) the coordination of the whole proposed method maintains the measured signal against strong in-band interference with the frequency is very close or even equal to that of the measured signal.

The rest of this paper is organized as follows. Section 2 gives an overview of the proposed method and the detailed design of three units, i.e. CM, ANBF and SDFA. In section 3, the implementation of the proposed method is presented. Simulation tests, the setup of a test prototype and the laboratory tests are shown in section 4. Section 5 draws the conclusion.

2. Design principle of proposed method

The block diagram of a typical transmissive/reflective sensor is shown in Fig. 1. Three key units of the proposed sensor, i.e. CM, SDFA, and ANBF, are shown in the dashed box. For the sake of clarification, the signals are defined as follows: transmitted signal is the signal emitted by the transmitter to the measurand; measured signal is the one responding to the physical variables of the measurand; interfering signal is the signal transduced by the receiver and responding to the interference; received signal is the mixture of the measured signal and interfering signal; and conditioned signal is the output signal of ANBF.
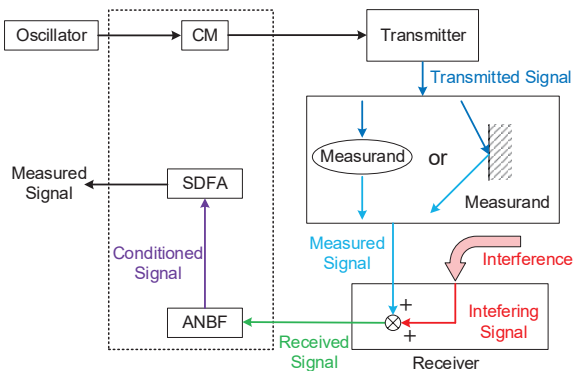

Figure 1: Block diagram of a transmissive/reflective sensor embedded with the proposed method

The CM circularly generates an amplitude or phase modulated signal according to the designed time-sequence requirement of the SDFA. The passband of the ANBF is cho-

sen to be narrow enough to ensure the conditioned signal only contains the measured signal and one in-band interfering component with a frequency quite close to that of the measured signal. By using the properties of odd/even functions, SDFA estimates and filters out the in-band interfering component in the conditioned signal. Then SDFA can obtain amplitude and phase of the measured signal similar to the idea of active or reactive power definitions in A.C. circuit. Details of the operating principle of three units are given in the following subsections.

2.1. Coordinated modulator

The schematic diagram of CM is shown in Fig. 2. CM is configured with two SPDT switches with control signals $g_1(t)$ (=0 or 1) and $g_2(t)$ (=0 or -1), respectively.
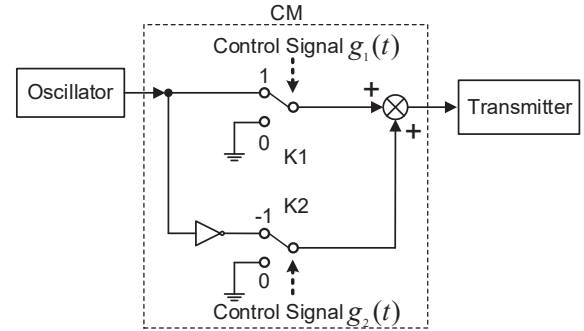

Figure 2: Schematic diagram of the coordinated modulator

Modulation index $\mu(t)$ of the CM is the sum of $g_1(t)$ and $g_2(t)$ and a piecewise function with values [1, 0, -1] as:

$$\mu(t) = g_1(t) + g_2(t) \tag{1}$$

Correspondingly, the CM can operate in one of the three modes defined in Table 1, i.e. full-amplitude modulation (f-AM), zero-amplitude modulation (z-AM), and π-phase modulation (π-PM). Particularly, when the CM is in z-AM mode, $\mu(t) = 0$ and the receiver only collects the interfering signal. Note that the mode $g_1(t) = 1$ and $g_2(t) = -1$ is not used as it provides same function as the z-AM mode.

Table 1
Modulation Modes and Index

$g_1(t)$	$g_2(t)$	Modes	$\mu(t)$
1	0	f-AM	1
0	-1	π-PM	-1
0	0	z-AM	0

The CM works circularly in a fixed time-sequence of five windows with the three modes as f-AM, f-AM, z-AM, f-AM and π-PM, as shown in Fig. 3. Each window includes a steady-state period T_{on} or T_{off} and a transient-state period T_{st}, respectively marked in green and red. When CM switches from one mode to another, the analog circuits will have a transient process. During the period of T_{st}, sampling is disabled. After the transient process, the conditioned signal reaches steady-state and the sampling is enabled at the

five windows defined as I-A, II-A, III, II-B and I-B. Note that between the windows I-A and II-A, no switching is needed. For consistency and symmetry, a virtual T_{st} is configured.
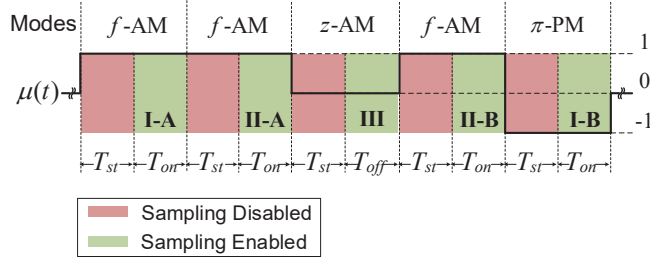

Figure 3: Time-sequence of CM

Since the transmitted signal is modulated by $\mu(t)$, the measured signal $s(t)$ is also modulated and the received signal $e_r(t)$ can be represented as:

$$\begin{cases} s(t) = \mu(t)A_s\sin(2\pi f_s t + \varphi_s) \\ e_r(t) = s(t) + e_n(t) \end{cases} \quad (2)$$

where A_s, f_s and φ_s are the amplitude, frequency and phase of $s(t)$, respectively; and $e_n(t)$ is the interfering signal.

2.2. Analog narrow-band filter

The ANBF is configured with an Nth-order multiple feedback circuit and its block diagram is shown in Fig. 4. As the ANBF should retain the measured signal, the frequency of the measured signal is chosen as the center frequency. Moreover, because the ANBF needs to maximize the suppressing effect of the interfering signal, an ideal ANBF can forcefully reject the interfering components in its stopband (with -40 dB attenuation in the application case). The passband of the ANBF in this paper is designed to be narrow enough so that the ANBF only allows the interfering signals with the frequencies mostly close to that of the measured signal to pass it. And this study is based on the assumption that the interfering signal passing the ANBF is a sinusoidal signal.
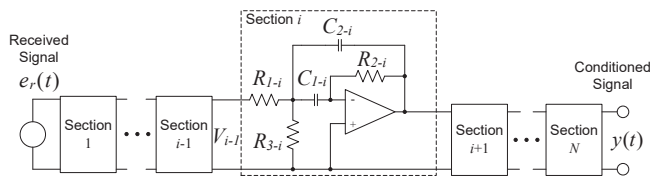

Figure 4: Schematic diagram of the narrow-band analog filter

In the output port of the ANBF, the conditioned signal $y(t)$ only contains the measured signal $s(t)$ and the in-band interfering component $n(t)$ as:

$$\begin{cases} n(t) = A_n\sin(2\pi f_n t + \varphi_n) \\ y(t) = s(t) + n(t) \end{cases} \quad (3)$$

where A_n, f_n, and φ_n are amplitude, frequency and phase in-band interfering signal $n(t)$.

Algorithm 1 Smart digital filtering algorithm

1: Sample data $\{y_{I,A}[k]\}$, $\{y_{II,A}[k]\}$ and $\{y_{III}[k]\}$
2: Initialize the parameters $\hat{A}_n^{(0)}$, $\hat{\theta}_n^{(0)}$, $\hat{\psi}_n^{(0)}$ based on (5)
3: **repeat**
4:     Construct cost function $J^{(i)}$ based on (6)
5:     Update estimated variables $\hat{A}_n^{(i)}$, $\hat{\theta}_n^{(i)}$, $\hat{\psi}_n^{(i)}$ based on (7)
6: **until** Convergence **return** $\hat{A}_n$, $\hat{\theta}_n$, $\hat{\psi}_n$
7: Sample data $\{y_{II,B}[k]\}$ and $\{y_{I,B}[k]\}$
8: Select symmetric data segments based on (14)
9: Generate virtual sampled data $\{\hat{n}_{I,A}[k]\}$, $\{\hat{n}_{II,A}[k]\}$, $\{\hat{n}_{II,B}[k]\}$ and $\{\hat{n}_{I,B}[k]\}$ to cancel the in-band interfering component in the sampled data of data segments based on (15)
10: Generate odd function data $\{u_{II,A}[k]\}$ and $\{u_{II,B}[k]\}$ in (16)
11: Calculate active component P based on (17) (19)
12: Generate odd function data $\{v_{I,A}[k]\}$ and $\{v_{I,B}[k]\}$ in (20)
13: Calculate reactive component Q based on (21)
14: Extract measured signal parameters A_s, φ_s' in (22)
15: **return** A_s, φ_s'

2.3. Smart digital filtering algorithm

The operation procedures of the SDFA are shown in Algorithm 1.

At each cycle, the SDFA will employ the conditioned signal $y(t)$ as the input, which are sampled from the five successive windows of the coordinated time-sequence. The sampled data of the windows I-A, II-A, III, II-B and I-B are represented as $\{y_{I,A}[k]\}$, $\{y_{II,A}[k]\}$, $\{y_{III}[k]\}$, $\{y_{II,B}[k]\}$ and $\{y_{I,B}[k]\}$, respectively, as shown in Fig. 5. The lengths of the windows are labeled as N_{on}, N_{on}, N_{off}, N_{on} and N_{on}. The time of $y_{I,A}[0]$ is defined as $t = 0$.
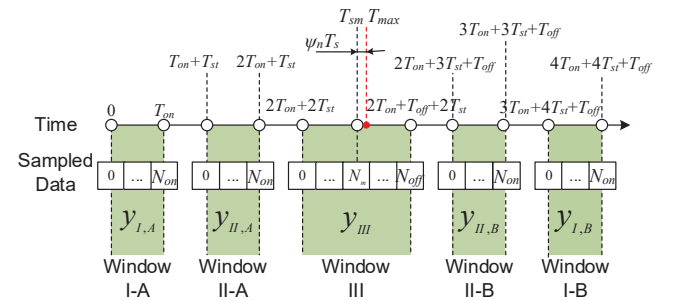

Figure 5: Sampled data in time-sequence

2.3.1. Estimation of in-band interfering component parameter

Note that within the window III in Fig. 3, the transmitter stops transmitting signal and then the conditioned signal only includes the in-band interfering component. So the sampled data $\{y_{III}[k]\}$ are used to estimate parameters of the in-band interfering component. Let $y_{III}[N_m]$ represent the point with the maximum value of $\{y_{III}[k]\}$. $y_{III}[N_m]$ is the value of the point sampled at the sampling instant $t = T_{sm}$, closest to the moment $t = T_{max}$ when the $n(t)$'s

maximum value occurrs (the red point in Fig. 3). Define T_s as the sampling period, and then we have $T_{max} - T_{sm} = \psi_n T_s$, where $-0.5 < \psi_n < 0.5$. Thus $y_{III}[k]$ can be rewritten as:

$$y_{III}[k] = A_n \cos[\theta_n(k - N_m - \psi_n)] \tag{4}$$

where $k = 0 : N_{off}$; and $\theta_n = 2\pi f_n T_s$. According to (4), the initial parameters can be calculated by using three sampled data $y_{III}[N_m - N]$, $y_{III}[N_m]$ and $y_{III}[N_m + N]$ as:

$$\begin{cases} \hat{\theta}_n^{(0)} = \dfrac{1}{N} \arccos(\dfrac{y_{III}[N_m - N] + y_{III}[N_m + N]}{2 y_{III}[N_m]}) \\ \hat{\psi}_n^{(0)} = \dfrac{1}{\hat{\theta}_n^{(0)}} \arcsin(\dfrac{y_{III}[N_m - N] - y_{III}[N_m + N]}{2 \sin(\hat{\theta}_n^{(0)} N)}) \\ \hat{A}_n^{(0)} = \dfrac{y_{III}[N_m]}{\cos(\hat{\theta}_n^{(0)} \hat{\psi}_n^{(0)})} \end{cases} \tag{5}$$

where N is a positive integer and satisfies: $M_m - N > 0$ and $M_m + N < N_{off}$.

The gradient descent method is adopted to estimate $\hat{A}_n$, $\hat{\theta}_n$ and $\hat{\psi}_n$ by fitting $\{y_{III}[k]\}$ based on a cosine function. The cost function $J^{(i)}$ is defined as:

$$\begin{cases} F^{(i)}(\hat{A}_n, \hat{\theta}_n, \hat{\psi}_n, k) = \hat{A}_n^{(i)} \cos[\hat{\theta}_n^{(i)}(k - N_m - \hat{\psi}_n^{(i)})] - y_{III}[k] \\ J^{(i)}(\hat{A}_n, \hat{\theta}_n, \hat{\psi}_n) = \displaystyle\sum_{k=0}^{N_{off}} [F^{(i)}(\hat{A}_n, \hat{\theta}_n, \hat{\psi}_n, k)]^2 \end{cases} \tag{6}$$

The estimated $\hat{A}_n^{(i)}$, $\hat{\theta}_n^{(i)}$ and $\hat{\psi}_n^{(i)}$ are updated as:

$$\begin{cases} \hat{A}_n^{(i+1)} = \hat{A}_n^{(i)} - \dfrac{\partial J^{(i)}}{\partial \hat{A}_n^{(i)}} \alpha_A \\ \hat{\theta}_n^{(i+1)} = \hat{\theta}_n^{(i)} - \dfrac{\partial J^{(i)}}{\partial \hat{\theta}_n^{(i)}} \alpha_\theta \\ \hat{\psi}_n^{(i+1)} = \hat{\psi}_n^{(i)} - \dfrac{\partial J^{(i)}}{\partial \hat{\psi}_n^{(i)}} \alpha_\psi \end{cases} \tag{7}$$

where α_A, α_θ and α_ψ are the step sizes of $\hat{A}_n^{(i)}$, $\hat{\theta}_n^{(i)}$ and $\hat{\psi}_n^{(i)}$, respectively. And the convergence criterion is defined as:

$$\begin{cases} \left| \hat{A}_n^{(i)} - \hat{A}_n^{(i-1)} \right| < \varepsilon_A \\ \left| \hat{\theta}_n^{(i)} - \hat{\theta}_n^{(i-1)} \right| < \varepsilon_\theta \\ \left| \hat{\psi}_n^{(i)} - \hat{\psi}_n^{(i-1)} \right| < \varepsilon_\psi \end{cases} \tag{8}$$

where ε_A, ε_θ and ε_ψ are small positive thresholds. The estimated results are respectively defined as $\hat{A}_n$, $\hat{\theta}_n$, and $\hat{\psi}_n$.

The estimated in-band interfering component $\hat{n}(t)$ can be reconstructed based on $\hat{A}_n$, $\hat{\theta}_n$, and $\hat{\psi}$ as:

$$\hat{n}(t) = \hat{A}_n \cos[\hat{\theta}_n(\frac{t - \hat{T}_{max}}{T_s})] \tag{9}$$

where $\hat{T}_{max} = 2T_{on} + 2T_{st} + (N_m + \hat{\psi}_n)T_s$ represents the estimated moment of $n(t)$'s maximum value occurring. Assume that in-band interfering signal during one cycle of the designed time-sequence is stationary, $n(t)$ can be rewritten as:

$$n(t) = A_n \cos[\theta_n(\frac{t - T_{max}}{T_s})] \tag{10}$$

Moreover, if the step sizes and the tolerances in the estimation are chosen properly, the estimated parameters can be approximated as: $\hat{A}_n \approx A_n$ and $\hat{\psi}_n \approx \psi_n$. However, the difference between θ_n and $\hat{\theta}_n$ cannot be neglected. Hence the subtraction error $\Delta n(t)$ is defined as the difference between $n(t)$ and $\hat{n}(t)$ as:

$$\begin{aligned} \Delta n(t) &= n(t) - \hat{n}(t) \\ &\approx 2\overline{A}_n \sin(\frac{\theta_n - \hat{\theta}_n}{2} k') \sin(\frac{\theta_n + \hat{\theta}_n}{2} k' + \delta) \end{aligned} \tag{11}$$

where

$$\begin{cases} k' = \dfrac{t - \hat{T}_{max}}{T_s} \\ \overline{A}_n = \dfrac{\sqrt{A_n^2 + \hat{A}_n^2 + 2 A_n \hat{A}_n \cos[\theta_n(\hat{\psi} - \psi)]}}{2} \\ \delta = \arctan\dfrac{A_n \sin[\theta_n(\hat{\psi} - \psi)]}{A_n \cos[\theta_n(\hat{\psi} - \psi)] + \hat{A}_n} \approx 0 \end{cases} \tag{12}$$

Here $\Delta n(t)$ is an approximate even function with respect to the vertical axis $t = \hat{T}_{max}$. Also, the measured signal $s(t)$ can be rewritten as:

$$s(t) = \mu(t) A_s \sin[\theta_s(\frac{t - \hat{T}_{max}}{T_s}) + \varphi_s'] \tag{13}$$

where $\theta_s = 2\pi f_s T_s$, usually known in a specific detector; and $\varphi_s' = \varphi_s + \theta_s \dfrac{\hat{T}_{max}}{T_s}$, denoting the phase of the measured signal $s(t)$ at $t = \hat{T}_{max}$.

2.3.2. Subtraction of in-band interfering component

Four equal-length data segments $\{y_{I,A}[M_1], \dots, y_{I,A}[M_2]\}$, $\{y_{II,A}[M_3], \dots, y_{II,A}[M_4]\}$, $\{y_{II,B}[M_4'], \dots, y_{II,B}[M_3']\}$ and $\{y_{I,B}[M_2'], \dots, y_{I,B}[M_1']\}$ are selected from the sampled data in the windows I-A, II-A, II-B, I-B, respectively. The data segments I-A and I-B are symmetric with respect to $t = \hat{T}_{max}$; also, the data segments II-A and II-B are symmetric with respect to $t = \hat{T}_{max}$. Hence M_j and M_j' ($j = 1$, 2,3, or 4) should satisfy:

$$M_j + M_j' = N_{on} - N_{off} + 2N_m + \lceil 2\hat{\psi}_n - 0.5 \rceil \tag{14}$$

Besides, the time period of each segment is composed of multiple periods of the measured signal.

Correspondingly, virtual sampled data $\{\hat{n}_{I,A}[k]\}$, $\{\hat{n}_{II,A}[k]\}$, $\{\hat{n}_{II,B}[k]\}$, and $\{\hat{n}_{I,B}[k]\}$ can be generated based on (9).

Then the virtual sampled data are subtracted from the sampled data in corresponding segments point by point as:

$$r_{w,x}[k] = y_{w,x}[k] - \hat{n}_{w,x}[k] = s_{w,x}[k] + \Delta n_{w,x}[k] \quad (15)$$

where w can be I or II; x can be A or B; $r_{w,x}[k]$ is defined as the residual sampled data; $s_{w,x}[k]$ is discrete data of the measured signal $s(t)$; and $\Delta n_{w,x}[k]$ is the discrete data of $\Delta n(t)$.

According to (11) (14), $\Delta n_{I,A}$ and $\Delta n_{I,B}$ are even symmetric with respect to $t = \hat{T}_{max}$. Similarly, $\Delta n_{II,A}$ and $\Delta n_{II,B}$ are also even symmetric.

2.3.3. Extraction of measured signal

The following properties of even and odd functions are used to remove the effect of subtraction error: 1) the product of an even function and an odd function is an odd function; and 2) the integral of an odd function in a symmetric interval with respect to the y-axis is 0.

An odd function $u(t)$ with respect to $t = \hat{T}_{max}$ is contructed as:

$$u(t) = \sin[\theta_s(\frac{t - \hat{T}_{max}}{T_s})] \quad (16)$$

where the frequency equals the measured signal's. Then two series of virtual sampled data $\{u_{II,A}[k]\}$ and $\{u_{II,B}[k]\}$ in the segments II-A and II-B are generated based on (16). Furthermore, active power component P is defined as the sum of the products $r_{II,A}[k]u_{II,A}[k]$ and $r_{II,B}[k]u_{II,B}[k]$ as:

$$P = \sum_{k=M_3}^{M_4} r_{II,A}[k]u_{II,A}[k] + \sum_{k=M_4'}^{M_3'} r_{II,B}[k]u_{II,B}[k] \quad (17)$$

As $\{\Delta n_{II,A}[k]\}$ and $\{\Delta n_{II,B}[k]\}$ are even symmetric, the products $\{\Delta n_{II,A}[k]u_{II,A}[k]\}$ and $\{\Delta n_{II,B}[k]u_{II,B}[k]\}$ are odd symmetric. So the sum of the products in the two windows is 0:

$$\sum_{k=M_3}^{M_4} \Delta n_{II,A}[k]u_{II,A}[k] + \sum_{k=M_4'}^{M_3'} \Delta n_{II,B}[k]u_{II,B}[k] \approx 0 \quad (18)$$

According to (15) (18), the effect of $\{\Delta n_{II,A}[k]\}$ and $\{\Delta n_{II,B}[k]\}$ can be removed. (17) can be transformed into:

$$P \approx \sum_{k=M_3}^{M_4} s_{II,A}[k]u_{II,A}[k] + \sum_{k=M_4'}^{M_3'} s_{II,B}[k]u_{II,B}[k] \\ = A_s\cos\varphi_s'(M_4 - M_3) \quad (19)$$

Similarly, another virtual odd function $v(t)$ is constructed as:

$$v(t) = \mu(t)\cos[\theta_s(\frac{t - \hat{T}_{max}}{T_s})] \quad (20)$$

And virtual sampled data $\{v_{I,A}[k]\}$ and $\{v_{I,B}[k]\}$ are generated depending on (20) in the segments I-A and I-B. Hence the reactive power component Q is defined as the sum of the products $r_{I,A}[k]u_{I,A}[k]$ and $r_{I,B}[k]u_{I,B}[k]$ as:

$$Q = \sum_{k=M_1}^{M_2} r_{I,A}[k]v_{I,A}[k] + \sum_{k=M_2'}^{M_1'} r_{I,B}[k]v_{I,B}[k] \\ \approx \sum_{k=M_1}^{M_2} s_{I,A}[k]v_{I,A}[k] + \sum_{k=M_2'}^{M_1'} s_{I,B}[k]v_{I,B}[k] \\ = A_s\sin\varphi_s'(M_2 - M_1) \quad (21)$$

According to (19) (21), P and Q are orthogonal to each other. Thus similar to the power calculation in A.C. circuit, the the measured signal's amplitude A_s and phase φ_s' can be extracted as:

$$\begin{cases} A_s = \frac{1}{M_1 - M_2}\sqrt{P^2 + Q^2} \\ \varphi_s' = \arctan\frac{Q}{P} \end{cases} \quad (22)$$

In summary, the above sections of the SDFA perform the following functions, respectively: the in-band interfering component estimation calculates the amplitude, frequency and the maximum point location of the in-band interfering component; instead of aiming at completely canceling the interference as the previous studies, the in-band interfering component subtraction partly reduces the interference and constructs the subtraction error as an even function; on the basis of the estimation and subtraction, the cancellation utilizing odd/even function properties can further remove the subtraction error effectively; and then the amplitude and phase of the measured signal are extracted using the power definitions in A.C. circuit.

3. Implementation of proposed method

This section introduces the hardware and software implementation of the proposed method, where a sinusoidal signal with 800 Hz frequency serves as the measured signal.

3.1. Implementation of coordinated modulator

Fig. 6 shows the schematic diagram of the CM, which is composed of four switch sections K1, K2, K3 and K4. When K1 and K2 are on, and K3 and K4 are off, the CM operates in f-AM mode; when K1 and K2 are off, and K3 and K4 are on, the CM operates in π-PM mode; and the CM will operates in z-AM mode when all the switch sections are off.
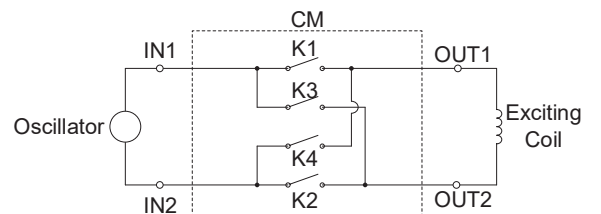

Figure 6: Equivalent Circuit of CM

Fig. 7(a) shows the switch section circuit, and section number i can be 1, 2, 3 or 4. The terminals T-i and the corresponding common terminals COM-i are respectively connected to the T-i and COM-i in Fig. 7(b).
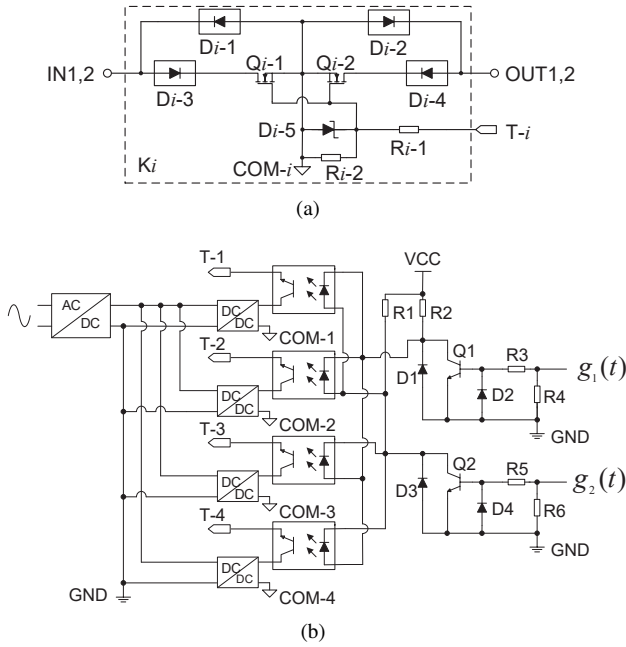

(a)

(b)

Figure 7: Schematic diagrams of a) switch section and b) control and power supply circuit

The states of the switch sections depend on the modulation control signals $g_1(t)$ and $g_2(t)$, which are generated by the main controller according to the time sequence in Fig. 3. Besides, since the DC/DC power supplies are isolated from each other, the common terminals are isolated.

3.2. Implementation of analog narrow-band filter

The ANBF for the 800 Hz measured signal is designed as an 8th-order Butterworth bandpass filter with the circuit given in Fig. 4. The selected operational amplifier is OPA 4227UA. The resistor values (Ω) are listed in Table 2, and all the capacitor values are 100 nF.

Table 2
Parameters of ANBF components

i	R_{i-1}	R_{i-2}	R_{i-3}
1	23.2k	82.5	49.9k
2	22.6k	78.7	48.7k
3	23.7k	34.8	124k
4	22.1k	32.4	115k

The frequency response curve of the ANBF is given in Fig. 8 based on 40 experimental test results, where the test signal frequency is from 670 to 973 Hz. $f_{c1} = 767$ Hz and $f_{s2} = 822$ Hz are the -3 dB cutoff frequencies. And $f_{s1} = 699$ Hz and $f_{s2} = 903$ Hz are the -40 dB stopband cutoff frequencies.
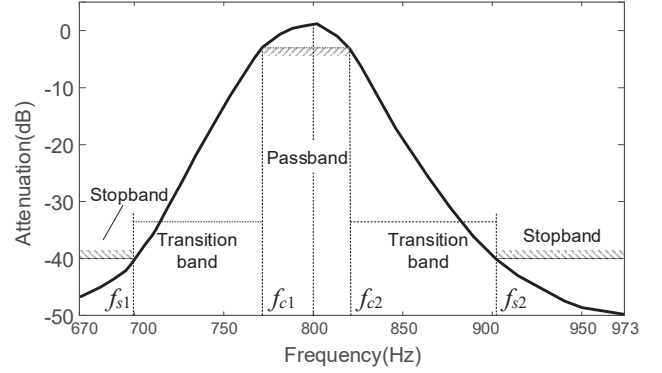

Figure 8: ANBF's frequency response

3.3. Implementation of smart digital filtering algorithm

The data acquisition and software implementation of the SDFA are based on DSP TMS320F28335 and ADC AD7606, respectively, as shown in Table 3.

Table 3
Parameters of DSP implementation

Chip	Parameter	Value
TMS320F28335	Sampling Rate	80kS/s
	Compution Accuracy	double
AD7606	Input Range	-5 V to +5 V
	Resolution	16 bits

3.3.1. Simulations of SDFA

The parameters of the SDFA are given in Table 4. And the SDFA is verified via simulation. In the simulation, the input signal is digitalized as integers based on the resolution of the real ADC. Thus the quantization error is taken into consideration. The amplitude and frequency range of the in-band interfering component are set as 0.5 V and between 700 Hz to 900 Hz, respectively; and the amplitude and frequency of the measured signal are set as 0.01 V and 800 Hz, respectively.

Table 4
Parameters of SDFA

Type	Parameter	Value
Steps and Thresholds in (7) (8)	α_A	2.8×10^{-3}
	α_θ	1.15×10^{-6}
	α_ψ	4.98
	ϵ_A	8×10^{-5}
	ϵ_θ	1.57×10^{-4}
	ϵ_ψ	8×10^{-3}
Time Periods in Fig. 3	T_{on}	0.0125s
	T_{off}	0.001825s
	T_{st}	0.03125s

One of the simulation tests is presented in Fig. 9. The in-band interfering signal's frequency is 824.47 Hz. Fig. 9 shows the $\hat{A}_n$, $\hat{\theta}_n$, and $\hat{\psi}_n$ and the extracted amplitude A_s of the measured signal corresponding to the iteration number

(0:10) respectively (represented as the blue line); and the real values of those parameters are shown as the red dashed line.
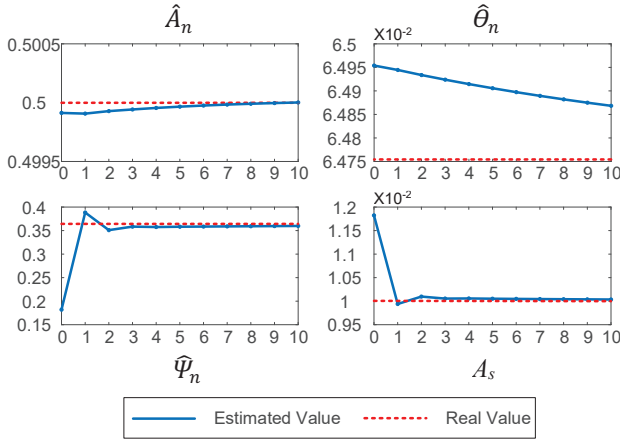

Figure 9: Parameter updates and extracted amplitude

The results show that the estimation of the in-band interfering component (step 5-8 in Algorithm 1) can converge to the real values of the estimated parameters after 6 times of iterations. Moreover, according to the update tendency, we find that the estimation accuracy of A_s is mainly determined by the estimation accuracy of ψ_n, while is less sensitive to the estimation accuracy. Then based on the estimated value of ψ_n, the estimation error of the frequency is calculated as 1.79 Hz/ 824.47 Hz. It is shown that when there is relatively large estimation error of the interference frequency, the SDFA can still give a satisfactory result of $A_s = 0.010038$ V with 0.38% error.

Moreover, as shown in Fig. 10, the maximum amplitude of the subtraction error $\Delta n(t)$ in the windows I-A, II-A, II-B and I-B is around 0.4815 V. Hence the in-band interfering component subtraction is of limited use in reducing the interference effect. And $\Delta n(t)$ is approximately even symmetrical. So the waveform further states the significant effect of the cancellation using the odd/even function properties.
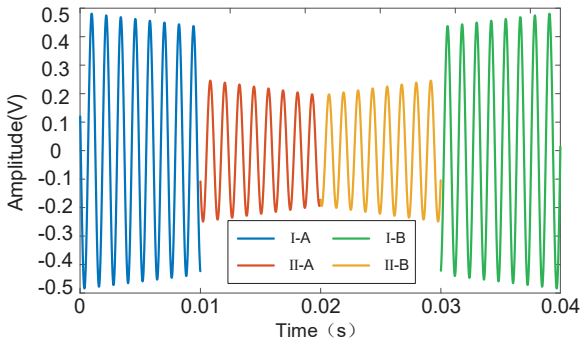

Figure 10: Subtraction error of subtraction procedures in SDFA

To further verify the generality of the algorithm, in total 2001 tests have been carried out via setting up the frequency of the interfering signal from 700.0 Hz to 900.0 Hz with step size 0.1 Hz, and 10 repeated simulations for each test. And in each simulation, the in-band interfering signal is set with random initial phase. In each simulation, we record two results i.e. the attenuation after only performing the procedures of the in-band interfering component subtraction and that after performing the complete SDFA. The conventional subtraction procedures of the in-band interfering component achieve the mean attenuations mostly ranging between -5 and -15 dB, as shown in Fig. 11(a). The attenuations of the complete SDFA exceed -76 dB in all simulation tests and most results are in the range between -80 and -90 dB as shown in Fig. 11(b). The results indicate that: 1) the procedures of the in-band interfering component subtraction cannot sufficiently reduce the strong in-band interference; 2) the major effect of the strong in-band interference can be removed by the cancellation using odd/even function properties; 3) the SDFA is robust to the in-band interference; and 4) most importantly, the SDFA can successfully reject the interfering signal with the frequency very close or even equal to that of the measured signal (800 Hz). The attenuation effect on the same-frequency interference is same as those on other in-band interference. Furthermore, the attenuation performances can be represented as the dashed envelope.
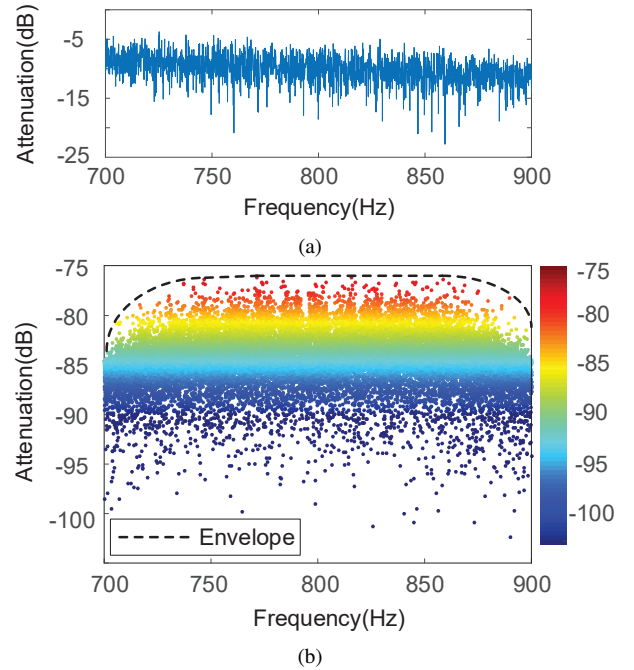

Figure 11: Attenuations on in-band interference after performing a) only subtraction procedures and b) complete SDFA

3.3.2. Comparisons with previous methods

The proposed method is compared with three previous methods: reverse-phase cancellation (RPC) in [9], adaptive noise cancellation (ANC) in [14] and spectral subtraction in [10]. The comparisons are carried out via simulations with the same setups in Section 3.3.1. The amplitude and frequency of the in-band interfering signal are set as 0.5 V and 824.47 Hz, respectively.

Similar to (11), the subtraction error $\Delta n(t)$ is defined as the difference between the in-band interfering signal and the canceling signal constructed by the above methods in this part. The $\Delta n(t)$ of the RPC is shown in Fig. 12(a). The RPC

estimates the interfering signal via FFT based on 65536 sampled points. The estimated frequency $\hat{f}$ is 823.98 Hz with higher accuracy than that in the SDFA, and then the amplitude of $\Delta n(t)$ of the RPC is distinctly smaller than that of the SDFA in Fig. 10. However, the error (95.59%) of A_s is exceedingly larger than that (0.38%) of the SDFA . Furthermore, we adjust the estimated frequency of the interference as 823.68Hz and 824.28 Hz to simulate the cases with lower or higher accuracy. The corresponding errors are 327.34% and 7.13%, respectively. The results show that the RPC relies more on the estimation accuracy of the interference frequency than the SDFA. And in the cases with such low SNR, the measurement error of the RPC might be very large.

In addition, the subtraction error of the ANC is shown in Fig. 12(b). In this case, optimized LMS algorithm is adopted on the weight calculations of the ANC. The subtraction error is less than 3×10^{-3} V. The results indicates that the ANC can accurately approach the in-band interfering signal without explicitly estimating the interference parameters. However, compared to the results of the SDFA (with 0.38% error), the ANC has a relatively larger measurement error (3.72%).
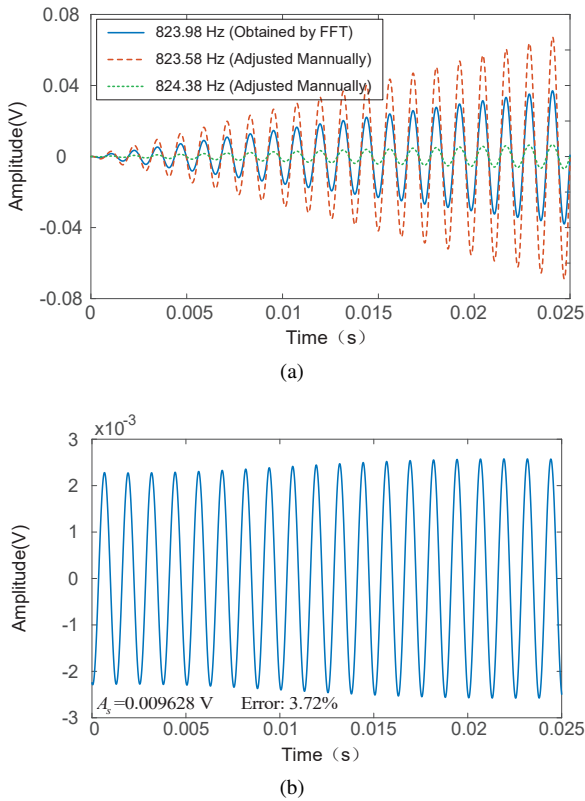

Figure 12: Subtraction errors of a) RPC and b) ANC

Fig. 13 presents the spectrums of the processed signal before and after the spectral subtraction. It is found that after performing the spectral subtraction, the frequency components from 820 Hz to 830 Hz, which represents the 824.47 Hz interference, are effectively removed. In contrast, the measured signal are well maintained. In comparison with the SDFA, the spectral subtraction is with a relatively lower

accuracy (1.25% error). Moreover, the spectral subtraction demands a higher computation cost. In this simulation, 16000 sampled points are used and Hamming window is applied.
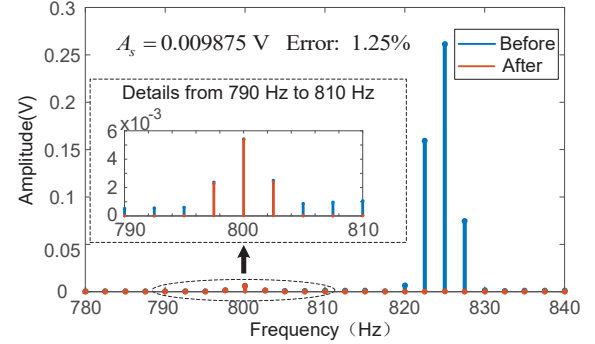

Figure 13: Spectrums before and after spectral subtraction

Additional tests of the ANC and spectral subtraction are carried out via setting up the frequency of the interfering signal from 700 Hz to 900 Hz with step size 5 Hz. The attenuations of the two methods is presented in Fig. 14, in comparison with the attenuations of the SDFA. It can be clearly observed that: 1) the attenuations of the ANC and spectral subtraction method are normally weaker than those of the SDFA; 2) when the frequency of the in-band interfering signal is extremely close or equal to that of the measured signal (from 785 to 810 Hz), the performances of the ANC and spectral subtraction will significantly decline.
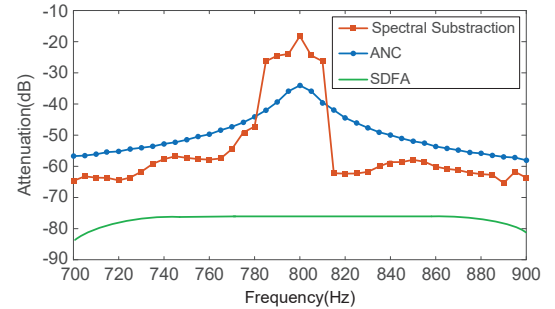

Figure 14: Performances of ANC, spectral subtraction and SDFA in 700 Hz to 900 Hz passband

In summary, the main advantages of the SDFA are: 1) the attenuations of the SDFA on the in-band interference is stronger than those of the above previous methods. 2) the SDFA has a higher accuracy in low-SNR cases; 3) the SDFA is robust to the estimation error of the interference frequency; and 4) the SDFA can forcefully cancel the interference with the frequency very close or equal to those of the measured signal.

4. Application case and laboratory tests

4.1. Application case

Electromagnetic detection of molten steel level in the mold of the continuous casting machine is a typical application of reflective sensors. The laboratory test platform in 15 is set up to test the proposed sensor in this special application
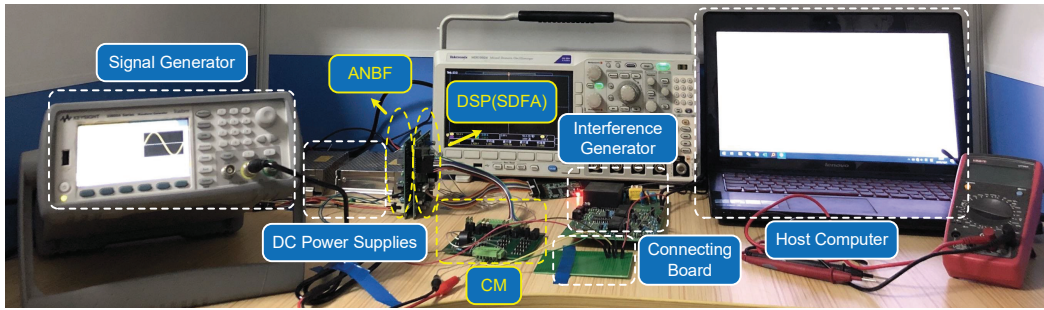
Figure 15: Test platform in laboratory

case. The diagram of an electromagnetic mold level detection system is shown in Fig. 16. The electromagnetic field generated by the exciting coil (transmitter) induces an eddy current in the molten steel and the surrounding conductive components. The resulting distribution of the eddy current electromagnetic field depends on the molten steel level in this mold. The reflected field induces a voltage in the sensing coils that serve as the receiver. And the frequencies of the exciting signal and inducing signal(the transmitted signal and received signal, respectively) are 800 Hz. The inducing voltage is in the range of 5 mV to 15 mV. CM is inserted between the oscillator and the exciting coil. ANBF and DSP (SDFA) are used to process the inducing signal.
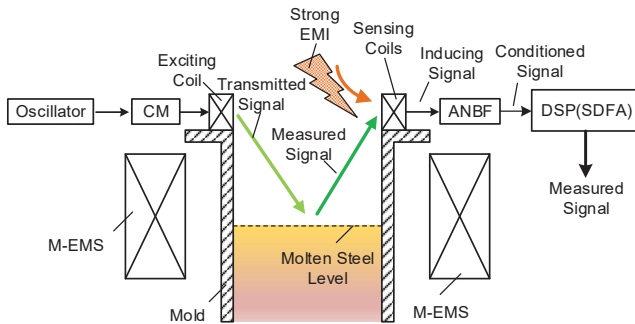

Figure 16: Diagram of an electromagnetic mold level detection system

Under M-EMS operating condition, the sensor is exposed to the strong electromagnetic interference generated by the M-EMS. So the sensor obtains a severely distorted signal and is likely to produce invalid sensing results without implementing the proposed method. The waveforms of the inducing voltage from the sensor installed at the real mold of the continuous casting machine is shown in Fig. 17.
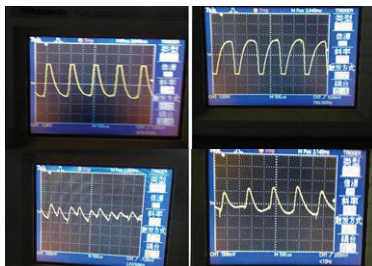

Figure 17: Waveforms of inducing voltage in filed tests

Those waveforms show that M-EMS generates a strong interfering signal with the following characteristics: 1) amplitude of the interfering signal ranges from 300 mV to 400 mV, which can be much stronger over that of the measured signal (5mV to 15mV); and 2) the interfering signal contains many frequency components and the main frequency is very close to that of the measured signal (800 Hz).

4.2. Laboratory tests

Parameters of the above case have been used to set up a test platform in the lab to implement and test the proposed sensor. As shown in Fig. 15, the platform consists of a signal generator, an interference signal generator, a connecting board, DC power supplies, a host computer, an oscilloscope, and the proposed sensor prototype which includes CM, ANBF and DSP for implementing the SDFA.

Here the signal generator generates the transmitted signal (800 Hz). The specially-made adjustable interference generator outputs the interfering signal. The exciting coil and the sensing coil are implemented by inductors installed on the connecting board, on which the interfering signal and measured signal are mixed via the addition circuit. The isolated AC/DC converters sipply dc power for the platform. The host computer collects and records the sensing data for analysis, via the test access port of the DSP.

The amplitude of input signal of the CM is set as 16 V. The output waveform of the CM in Fig. 18 is distorted due to the small voltage drops in diodes and FETs. And the output signal's spectrum in Fig. 19 indicates that the distorted signal is composed of the fundamental (800 Hz) and the additional odd harmonics components.
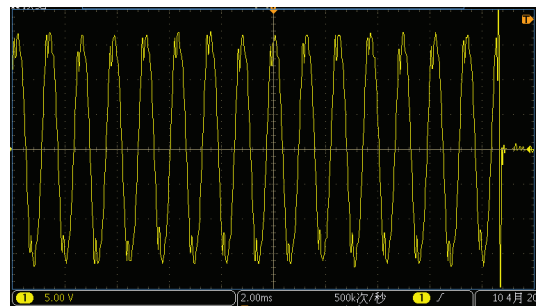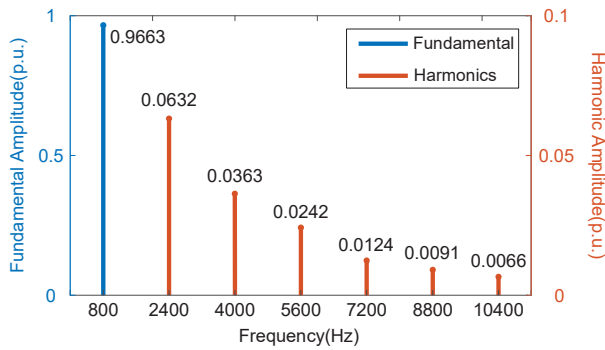

Figure 18: Output signal of CM

Figure 19: Output signal spectrum of CM

Let the modulated signal of the CM in Fig. 19 acts as the input of the ANBF. Its output signal in steady-state is sinusoidal, as shown in Fig. 20(a). ANBF can effectively reject the extra harmonics generated by the CM and mixed in the transmitted signal. Furthermore, in coordination with the CM, the ANBF's transient operation is shown in Fig. 20(b), in which the time horizon of the interval are annotated as: the data sampling enabled in T_{on} and T_{off}, and no data sampled in T_{st}.
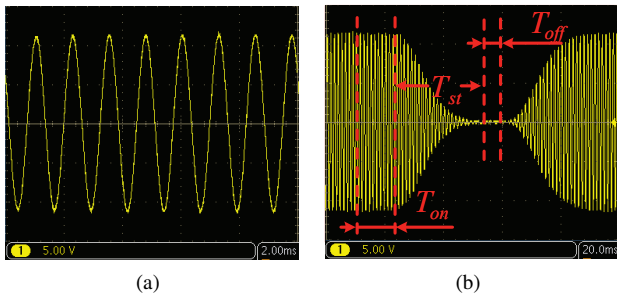

Figure 20: ANBF's output signal in a) steady-state, and b) transient operation

By adjusting the connecting board, the measured signal's amplitude is set as 0.0100 V ; and the interfering signal is adjusted to be with the 0.36 V amplitude and a main frequency very close to 800 Hz. The received signal is mixed by the two above signals, as shown in Fig. 21(a). The estimated amplitude and frequency of the in-band interfering component are calculated to be 0.3541 V and 803.74 Hz, which can be read the host computer. And the final calculation result of the measured signal's amplitude is 0.00996 V, and the measurement error is 0.4%. Moreover, the result is converted to an analog signal in Fig. 21(b) via DAC, which intuitively illustrates the effectiveness of the proposed method.
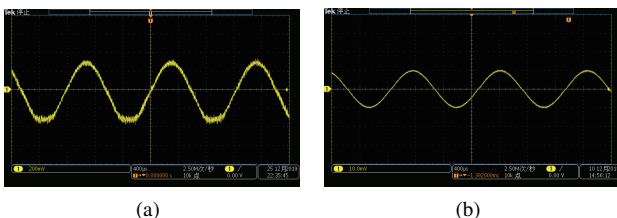

Figure 21: a) Received signal and b) analog ouput signal

Performance of the proposed method against stronger interference than those in Fig. 17 (0.3V to 0.4V) has been further validated. The interfering signals are divided into seven levels according to their amplitudes (0.4V, 0.5V, 0.6V, 0.7V, 0.8V, 0.9V and 1.0 V), with the corresponding SNR under the interference levels are (-32.04, -33.98, -35.56, -36.90, -38.06, -39.08 and -40 dB), respectively. At each level, 20 repeated tests are performed. And the frequency of in-band interfering component is adjusted randomly between 750Hz and 850 Hz, since those signals cannot be rejected by the ANBF. The results of those tests are summarised in Fig. 22, i.e. the maximum absolute errors (%) and mean absolute errors (%). The mean absolute errors of the extracted amplitude in all interference levels are less than 0.7%. Moreover, the maximum absolute error of all test results is 1.88%. If SNR>-32.04 dB, the maximum absolute error is less than 0.6%. When interference magnitude is less than 0.6 V (SNR> -35.56 dB), the maximum absolute error will not be over 1%. Overall, the results show the proposed method's robust performance under strong in-band interference conditions.
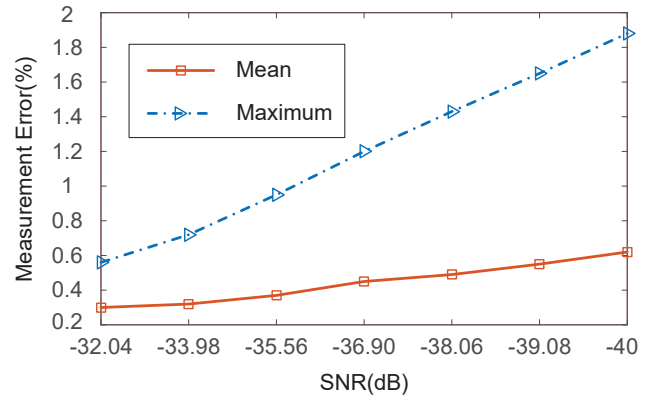

Figure 22: Absolute measurement error and subtraction attenuation in laboratory tests

5. Discussion

In this paper, we have shown that the proposed coordinated method has a strong effect on canceling in-band interference and high measurement accuracy. We proved that by using wave symmetry properties, the proposed method effectively eliminates the inevitable subtraction error in the previous time-domain interference cancellation methods. Also, we examined the robustness of the proposed method to remove the interferences with the frequencies very close or equal to that of the measured signal, which cannot be reduced by the previous frequency-domain interference cancellation methods. From the realistic implementation aspects, our method is suitable for the measurement demanding high accuracy. And the complexity of our method is relatively low. The analog filtering techniques are mature. Modulation techniques are also familiar in applications and its time-sequence can be designed based on the cases. And the SDFA is easy to implement in signal processors. The high sampling rate and high resolution of analog-to-digital converter and the high-performance signal processor contribute

to a short response time and high measurement accuracy of the proposed method.

The proposed method still has several limitations. The SDFA is designed to cancel only one in-band interfering signal, requiring a sufficiently narrow passband of the ANBF. And the ANBF satisfying the requirement tends to have a long transient period, leading to a relatively slow response speed. Moreover, we have not considered the possible scenarios with two or more in-band interfering signals. Further studies will focus on how to effectively implement the proposed method to deal with multiple in-band interferences. In addition, the proposed method cannot be applied on the measurement of non-sinusoidal signals at present.

6. Conclusion

This paper has proposed a novel coordinated detection method for transmissive/reflective sensor under the strong in-band interference condition. The proposed method designs three coordinated parts: a CM circularly modulating the original transmitted signal; an ANBF with a very narrow passband only passed by the measured signal and an in-band interfering component; and an SDFA estimating the parameters of the in-band interfering component, and then canceling the in-band interfering component by using the odd/even function properties. Finally, the amplitude and phase of the measured signal are extracted according to the power definitions in A.C. circuit. This method solves the failure due to the estimation error of the interference frequency and can give accurate sensing values in low-SNR scenarios, as the in-band interfering component is reconstructed based on the estimated maximum point and canceled based on the wave symmetry properties. Moreover, the proposed method can effectively reject the interfering signal with the frequency very close to or even equal to that of the measured signal.

Simulation tests show that the SDFA provides stronger cancellation on the in-band interference and has higher accuracy, in comparison with the previous time-domain cancellation method, adaptive noise cancellation method and spectral subtraction method. Moreover, based on more than 20000 simulations, SDFA's attenuations in the passband further demonstrates its outstanding robustness to all the in-band interfering signals with the attenuations exceeding -76 dB. Hardware and software implementation of a prototype has been built and tests are set up based on parameters of a real application case of electromagnetic mold level detection under the M-EMS operating condition. The experimental test results under different interference magnitude levels indicate the effectiveness of the proposed method, as when the in-band interference is less than 40 times stronger over the measured signal (SNR>-32.04 dB), the absolute error is less than 0.6%.

References

[1] Yang, H.Z., Qiao, X.G., Luo, D., Lim, K.S., Chong, W., Harun, S.W., 2014. A review of recent developed and applications of plastic fiber optic displacement sensors. Measurement 48, 333–345.

[2] Yang, Y., Yamazaki, K., Aoyama, H., Matsumiya, S., 2000. Fiber optic surface topography measurement sensor and its design study. Precision engineering 24, 32–40.

[3] Yang, T., Zhao, Q., How, K.Y., Xu, K., Lu, M., Xie, Y., Yin, W., 2017. Level measurement for saline with a small surface area using high frequency electromagnetic sensing technique. Measurement 101, 118–125.

[4] Rahman, H., Rahim, H., Ahmad, H., Yasin, M., Apsari, R., Harun, S.W., 2013. Fiber optic displacement sensor for imaging of tooth surface roughness. Measurement 46, 546–551.

[5] Prateek, G., Hurtado, M., Nehorai, A., 2017. Target detection using weather radars and electromagnetic vector sensors. Signal Processing 137, 387–397.

[6] Rivet, F., Veyrac, Y., Deval, Y., Garrec, P., 2016. Adaptive interference cancellation using a sampled analogue signal processor. IET Radar, Sonar Navigation 10, 43–49.

[7] Chen, B., Li, Y., Cao, X., Sun, W., He, W., 2019. Removal of power line interference from ecg signals using adaptive notch filters of sharp resolution. IEEE Access 7, 150667–150676.

[8] Yue, Y., Jiang, T., Han, C., Wang, J., Chao, Y., Zhou, Q., 2019. Suppression of periodic interference during tunnel seismic predictions via the hankel-svd-ica method. Journal of Applied Geophysics 168, 107–117.

[9] Zhou, W., Liu, Y., Li, G., Yan, G., Yang, S., Li, H., Zhou, C., Su, C.Q., 2014. Power frequency interference and suppression in measurement of power transmission tower grounding resistance. IEEE Transactions on Power Delivery 30, 1016–1023.

[10] Bozchalooi, I.S., Liang, M., 2008. A joint resonance frequency estimation and in-band noise reduction method for enhancing the detectability of bearing fault signals. Mechanical Systems and Signal Processing 22, 915–933.

[11] Firdauzi, A., Wirianto, K., Arijal, M., Adiono, T., 2013. Design and implementation of real time noise cancellation system based on spectral subtraction method. Procedia Technology 11, 1003–1010.

[12] Glover, J., 1977. Adaptive noise canceling applied to sinusoidal interferences. IEEE Transactions on Acoustics, Speech, and Signal Processing 25, 484–491.

[13] Ferdjallah, M., Barr, R.E., 1994. Adaptive digital notch filter design on the unit circle for the removal of powerline noise from biomedical signals. IEEE Transactions on Biomedical Engineering 41, 529–536.

[14] Wesson, K.D., Ochshorn, R.M., Land, B.R., 2009. Low-cost, high-fidelity, adaptive cancellation of periodic 60 hz noise. Journal of Neuroscience methods 185, 50–55.

[15] Zhu, Z., Gao, X., Cao, L., Pan, D., Cai, Y., Zhu, Y., 2016. Analysis on the adaptive filter based on lms algorithm. Optik 127, 4698–4704.

[16] So, H., 1997. Adaptive algorithm for sinusoidal interference cancellation. Electronics Letters 33, 1910–1912.

[17] Suarez, J., Kravtsov, K., Prucnal, P.R., 2011. Methods of feedback control for adaptive counter-phase optical interference cancellation. IEEE Transactions on Instrumentation and Measurement 60, 598–607.

[18] Luo, A., Xiao, H., Ouyang, H., Wu, C., Ma, F., Shuai, Z., 2012. Development and application of the two-phase orthogonal power supply for electromagnetic stirring. IEEE Transactions on Power Electronics 28, 3438–3446.

[19] Yang, Z.g., Wang, B., Zhang, X.f., Wang, Y.t., Dong, H.b., Liu, Q., 2014. Effect of electromagnetic stirring on molten steel flow and solidification in bloom mold. Journal of Iron and Steel Research International 21, 1095–1103.

[20] Kaur, M., Kakar, S., Mandal, D., 2011. Electromagnetic interference, in: 2011 3rd International Conference on Electronics Computer Technology, IEEE. pp. 1–5.

[21] Dunn, P.F., 2011. Fundamentals of sensors for engineering and science. Crc Press.

[22] Webster, J.G., Eren, H., 2018. Measurement, Instrumentation, and Sensors Handbook: Two-Volume Set. CRC press.

[23] Antoniou, A., 2016. Digital signal processing. McGraw-Hill.

Jie Teng received a B.S. degree from the School of Electrical and Electronic Engineering, Huazhong University of Science and Technology, Wuhan, China, in 2014, where he is currently pursuing a Ph.D. degree. His current research interests include power system operations and controls.

Shaorong Wang received a B.S. degree from Zhejiang University, Hangzhou, China, in 1984, M.S. degree from North China Electric Power University, Baoding, China, in 1990, and Ph.D. degree from the Huazhong University of Science and Technology, Wuhan, China, in 2004. He is currently a Professor with the School of Electrical and Electronic Engineering, HUST. His current research interests include power system operations and controls, smart grids, robotic applications, big data, and machine vision.

Lin Jiang received his B.S. and M.S. degrees in Electrical Engineering from the Huazhong University of Science and Technology, Wuhan, China, in 1992 and 1996,respectively; and his Ph.D. degree in Electrical Engineering from the University of Liverpool, Liverpool, ENG, UK, in 2001. He is presently working as a Reader of Electrical Engineering at the University of Liverpool. His current research interests include the optimization and control of smart grids, electrical machines, power electronics and renewable energy